# Molecular Tagging Velocimetry Characterization of Rapid KDP Crystal Growth

**D. Maynes**
Dept. of Mechanical Engineering, Brigham Young University, Provo, UT 84602

*Measurements of the tangential and axial velocities near the prism faces of a rotating mock crystal mounted on a rotating platform are presented. These measurements were made using molecular tagging velocimetry and are significant to the rapid growth of KDP crystals because they provide a description of the flow field and the evolution of the relative tangential and axial velocities near the prism faces and in the bulk flow region. These data represent the first measurements of fluid velocities around rotating crystal geometries, and thus provide a benchmark for future computer simulations of the crystal growth process at higher Re than previously obtainable. The measurements provide a temporal and spatial description of the evolving velocity field in the vicinity of a rotating crystal. Rotational conditions and locations on the prism faces where low shear rates are likely to occur, based on the measurements presented, are discussed qualitatively.*

## Introduction

It long has been recognized that both hydrodynamic behavior and kinetic phenomena are important in the growth process of single crystals from solution, and excellent reviews of these two areas have appeared in the literature (Chernov, 1974; Wilcox, 1983). Although there has been significant interest in quantifying the hydrodynamic behavior, a detailed understanding of the fluid dynamics associated with the growth process is lacking because spatially resolved measurements of the velocity field for such flows have not previously appeared. Measurements of the velocity field are critical, however, if the effects of changing parameters that alter the fluid dynamics (that is, rotation rate, acceleration rate, container size, etc.) on the growth process are to be well understood.

Due to their interesting nonlinear electrical and optical properties, $KH_2PO_4$ (KDP) and its isomorphs have recently been the subject of a wide variety of investigations (De Yoreo et al., 1996). KDP and its deuterated analog $KD_2PO_4$ (DKDP) are widely used to control the parameters of laser light such as pulse length, polarization, and frequency through the first- and second-order electrooptic effects (Nye, 1985). For the development of large laser systems, such as the National Ignition Facility (NIF), many large KDP and DKDP crystals are required (up to $50\times50\times50$ cm$^3$) for use as frequency converters and optical switches. Efficient operation of such devices also requires crystals with a high degree of perfection.

The focus of the present experimental work is to study the fluid mechanics associated with the rapid growth process for single crystals of KDP currently under investigation at Lawrence Livermore National Laboratory (LLNL). Because the growth rates obtained with rapid growth are about an order of magnitude greater than for traditional growth methods, understanding the fluid dynamical behavior is significantly more important. Rapid crystal growth differs from traditional diffusion-based processes by maintaining the solution at higher supersaturation levels and by the use of forced convection to enhance mass transport to the crystal. This approach is similar to the accelerated crucible rotation technique (ACRT) suggested by Scheel (Schulz-Dubois, 1971). At LLNL growth rates of 10–20 mm/day have been realized in both large ( $\sim$ 1000 L) and small ( $\sim$ 20 L) crystal-growth tanks where KDP crystals of approximate size $50\times50\times50$ cm and $17\times17\times17$ cm have been grown (Zaiteseva, 1997).

The flow field associated with the rapid growth of KDP crystals is unsteady, turbulent, and three-dimensional. It is generated by the rotation of a crystal, mounted on a platform, in a tank of solution. Stirring of the solution is accomplished by a periodic and reversing rotation schedule where subsequent reversals of direction are separated by a short time with no rotation. For each reversal of direction there exists a period of acceleration where the angular rotation rate is increasing, a period of constant rotation rate, and a period of

deceleration when the crystal comes to rest prior to reversal of direction. A typical rotation schedule in a 20-L tank would be a rotation rate of 1 rps (60 rpm) with an acceleration of 1 $rps^2$ (3600 $rpm^2$), and a period of 13 before reversal. The crystal is rotated and reversed periodically to cause agitation, and a time-averaged flow pattern that is similar for all faces of the crystal. Other methods of creating a time-averaged flow pattern with the crystal stationary (that is, an oscillating uniform flow) would not result in all faces of the crystal subject to the same hydrodynamics.

Such flow fields, although exhibiting some similarity, are significantly different from the commonly studied stirred-mixing-tank flows. One primary difference is that stirred mixing tanks operate primarily in a unidirectional environment (Tatterson, 1991) (the impeller does not reverse direction), whereas reversal of direction by the rotating crystal is fundamental to the crystal growth process. Also of note is that the geometries of typical mixing impellers are much simpler (Wu and Patterson, 1989) than the combination of crystal and support platform studied here (Figure 1). The most commonly studied mixing impellers are the six-bladed Rushton turbine and the pitched-blade Rushton turbine (Rutherford et al., 1996). Other impeller designs are also commonly studied, but the dimensions of most all impellers that appear in the literature, with regards to the ratios of impeller diameter to tank diameter and impeller blade height to tank diameter, are similar to those for the Rushton turbine. These ratios are typically between two and three with regards to impeller diameter and about 10 with regards to the blade height (Bertrand et al., 1980; Zhou and Kresta, 1996). Because of these major distinctions, other than general features of the flow fields (that is, establishment of secondary flows, existence of separated regions, etc.), comparisons with velocity-field data from mixing-tank studies are of little value.

Previous efforts to characterize the flow field associated with solution crystal growth have used either a theoretical, computational, or experimental approach. Many of the early efforts were of a theoretical nature. With regards to solution hydrodynamics, these approaches by necessity assume simplified flow behavior. Often two-dimensional models or order-of-magnitude analysis was utilized, providing general descriptions of flow-field patterns or assuming a velocity distribution for mass-transport analysis. However, these models lack detail of real three-dimensional flow-field behavior.

With dramatic advances in computational resources, computer simulations of three-dimensional and unsteady flow field are now becoming possible. Recently Derby and coworkers have successfully employed a computational approach enabling them to compute the time-varying flow field over 1 cycle for a rotating KDP crystal in solution (Zhou and Derby, 1997; Yeckel et al., 1998). This work is significant because it represents the first three-dimensional computational results over an entire tank volume. However, these results are limited to a Reynolds number ($Re$), based on a tank radius of $1.2 \times 10^3$, and experimental validation of the results has not occurred. In typical small-scale solution-growth tanks, the Reynolds number for rapid crystal growth is typically of the order $7 \times 10^4$, or some 60 times larger than the largest $Re$ at which computations have been performed. In large-scale crystal-growth tanks the Reynolds number may approach $1 \times 10^6$. Consequently, when considering rapid crystal growth, computer limitations thus far prohibit dynamically similar simulations of the crystal-growth process.

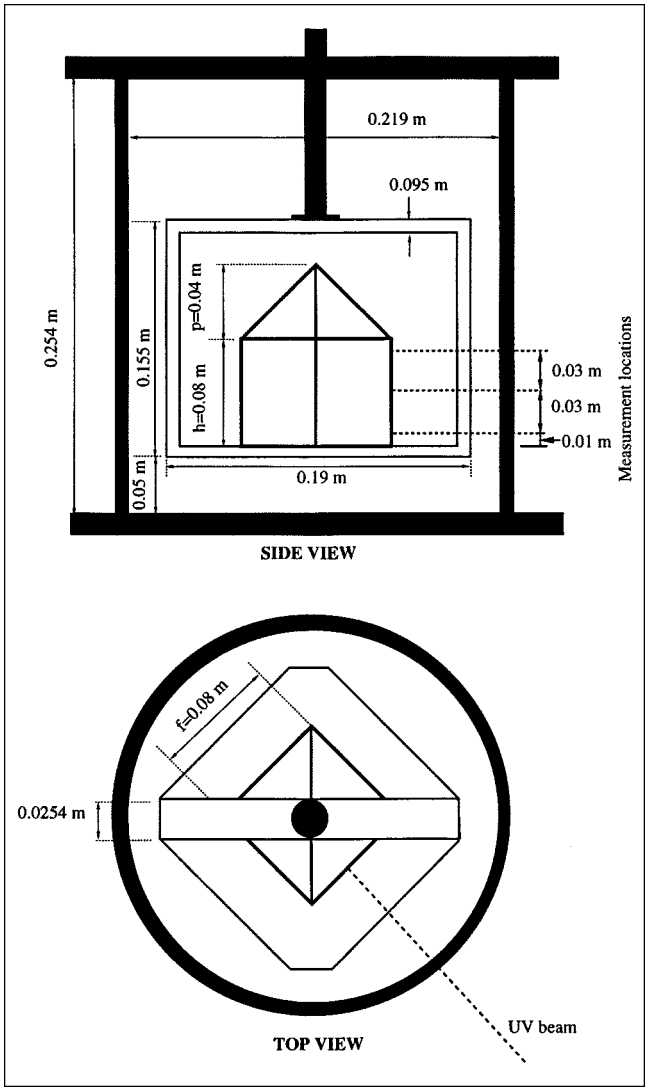


**Figure 1. Top and side views of the flow facility and mock crystal on the support platform.**

All relevant dimensions are shown in addition to the locations where velocity profiles were obtained.

Most previous experimental studies employed flow visualization to characterize the flow field for solution growth (Bordui and Motakef, 1989; Rashkovich and Shekunov, 1990). Such studies can give a three-dimensional picture of the flow field in a plane and thus provide valuable qualitative information. For typical studies, visualization is obtained in a laboratory reference frame. Consequently, for solution growth where the crystal is rotated, relating the observed flow field to a reference frame with respect to the crystal is quite difficult. Since it is the fluid velocity relative to the crystal that is important with regards to transport phenomena, the use of flow visualization alone is inadequate in quantifying flow-field behavior with respect to a rotating crystal.

In recent experimental studies (Maynes et al., 1997; Maynes et al., 1998) hydrodynamic scaling relations describing scale-

up from small to large tanks and the mixing dynamics associated with small and large crystals were presented. These studies focused on the evolution of global-flow features (torque and tangential velocity fluctuations in the bulk flow), but did not address spatial variations in the flow field. For rapid crystal growth these scalings are useful because they indicate how the turbulence level and transport of momentum scale with time, acceleration, rotation rate, crystal size, and tank size. They also provide information on how to maintain comparable mixing dynamics when scaling up from small to large crystals and from small to large tanks. Specifically, the data showed that regarding the temporal evolution of the flow field from startup, or upon reversal of direction, three distinct temporal regimes exist. The first regime was referred to as the buildup regime, where both the velocity fluctuations and torque remain approximately constant. In this regime, the crystal has no knowledge of the tank boundaries. In the second regime, referred to as the decay regime, the velocity fluctuations and torque decay with power-law relations as the effects of tank geometry impact. The final regime is steady state where the torque and velocity fluctuations level off to a mean level.

These previous studies are important with regards to maintaining a globally well-mixed solution; however, they do not address the behavior of the fluid velocity with respect to the rotating crystal. Spatially resolved velocity information near the rotating crystal surfaces is critical, however, with regards to the quality of the crystal surfaces. A common problem that is affected by the solution hydrodynamics is the formation of solute inclusions during growth (Zhou and Derby, 1997). Studies by Bordui (Bordui and Motakef, 1989) and Janssen-van Rosmalen et al. (Janssen-van Rosamalen and Bennema, 1977) have noted that there is some correlation between the generation of inclusions with the solutions hydrodynamics for KDP growth. Others have noted that the form of the fluid-velocity direction next to a crystal is important with regards to macrostep formation and stability. For example, stability analysis by Coriell et al., focusing on macrostep generation parallel to fluid motion has indicated that the magnitude and direction of the velocity gradient relative to the direction of step propagation on the vicinal surfaces can either promote or inhibit macrostep formation (Coriell et al., 1998). Related studies by Potapenko also show lateral perturbations of propagating macrosteps can be unstable to certain flow conditions dependent upon the velocity gradient (Potapenko, 1996). Both of these studies assumed steady-state flow, and no present theory addresses fluctuating transient flows. However, understanding of the velocity field near the crystal surface in addition to the global flow features is necessary and in due course should lead to better control of the growth process.

The experimental approach for the present study utilized a novel velocity measurement technique that allows quantification of fluid-velocity profiles next to a rotating crystal. Measurements of velocity profiles near the prism faces of a mock crystal were obtained using a technique called molecular tagging velocimetry (MTV). Utilization of MTV provides time-resolved measurements of either tangential, $V$, or axial (along the axis of rotation), $W$, velocity profiles in a fixed plane of the flow field. These provide the first spatially resolved measurements of velocity profiles near the prismatic surfaces of a rotating crystal, and velocity gradients along the profiles can be obtained. This article reports on these velocity measurements, describes the transient flow field, and discusses their relevance to the rapid crystal-growth process.

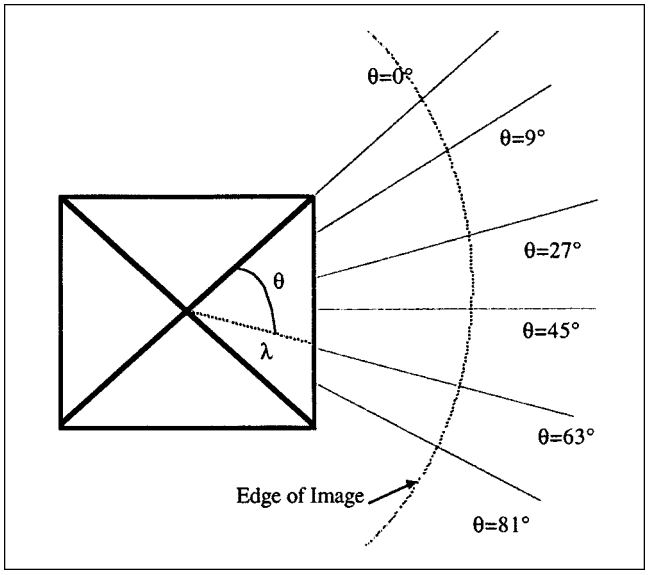


**Figure 2. Mock crystal rotating relative to an MTV line.**

## Methodology

### *Experimental setup*

Experiments were conducted in a flow facility of height, $H$, 0.254 m and diameter, $D$, 0.219 m; these dimensions match those of an actual 20-L crystal-growth tank employed at LLNL. The liquid used for the investigation was distilled water at 20°C. A variable-speed computer-controlled motor located directly above the tank connects to a shaft providing rotation to the mock crystals and support platform. The characteristic length, $L$, of the crystal is taken to be the distance from the center to a corner, or $L = f/2^{1/2}$, where if is the prism-face length. The height of the prism face is denoted by $h$, and the height of the pyramid cap is $p$. A mock crystal mounted on a Plexiglas platform in a tank is shown in Figure 1.

Tangential and axial velocity measurements were conducted at three vertical locations for a mock crystal with a prism face length of 0.08 m, height of 0.08 m, and a 0.04-m-tall pyramidal cap. The measurements resulted in a set of time series of the instantaneous velocity profiles obtained at 60 Hz and at the locations shown in Figure 2. These locations were 0.01 m above the support platform ($z^* = z/h = 0.125$), at midheight on the prism face ($z^* = 0.5$), and at 0.01 m below the top of the prism face ($z^* = 0.875$). At each of these locations rotation rates varying from 0.2 rps to 1.5 rps (12 rpm to 90 rpm) and acceleration rates of 0.01, 0.1, and 1.0 rps$^2$ (36, 360 and 3,600 rpm$^2$) were investigated.

### *Molecular tagging velocimetry*

A relatively new technique, called molecular tagging velocimetry, or MTV, was used for the measurement of the tangential and axial velocity profiles. The technique is termed

MTV following the suggestion of Gendrich and Koochesfahani (1996) (formerly it was called laser-induced photochemical anemometry, or LIPA). This technique has evolved from the first fluid-mechanic applications of light-sensitive chemicals in 1962 (Miller, 1962) to a powerful velocity measurement tool with contributions and improvements by a number of researchers. MTV conceptually and in practice is straightforward. The flow field of interest is first doped with a small concentration of photochemical. For this experimental program the photoluminescent chemical (1-BrNp·G$\beta$-CD·ROH ternary complex), developed by Ponce et al. (1993), was used. Using a Xybion ISG-250 camera, this chemical has an imageable phosphorescent ''lifetime'' of about 12 ms.

Velocity profiles are obtained by comparison of phosphorescent lines deformed by fluid motion with lines exhibiting no deformation. The optical configuration used to generate the phosphorescent lines involves dividing the UV laser beam into a series of approximately parallel lines. These lines are directed into an area of interest in the flow field perpendicular to the component of velocity to be measured. The laser fires, exciting the photochemical along the lines. The lines deform as the fluid flows, and after a few milliseconds a synchronized CCD camera shutters, capturing the deformed lines on video. The distance that each point along a line deforms is measured by comparing the undeformed and deformed lines. The velocity component normal to a line can be calculated by $V \approx \Delta x/\Delta t$, where $\Delta x$ is the distance between deformed and undeformed lines and $\Delta t$ is the time between the laser pulse and the time the camera shutters.

The velocity can be computed as just described for each pixel along the set of laser lines. The result is a set of instantaneous velocity profiles for each frame recorded by the camera. A single MTV line was used for the tangential and axial-velocity profile measurements presented here. For the present measurements a single camera system was employed. Thus, the axial and tangential velocities were not obtained simultaneously, but during separate experiments with identical conditions and line location. Errors in locating the line centers using the image analysis algorithms are typically on the order of 0.3 pixel for instantaneous velocities (Hill and Klewicki, 1996). This corresponds to an error in the velocity measurements of about $5\times10^{-3}$ (0.5 cm/s), and this is also the minimum velocity that can be resolved with the present setup. The spatial resolution for measurements in the tank was about $9.5\times10^{-5}$ m/pixel for all results, and the time delay between the laser pulse and camera shutter was typically about 5 ms. The radial length of the MTV profiles was about 0.025 m.

The line technique is susceptible to additional errors due to the radial velocity parallel to the MTV line for both the axial and tangential velocity measurements. This error results from the inability to identify and track unique fluid elements. For example, the tangential velocity is $V_\theta = R\Delta\theta/\Delta t$, where $R$ is the radial location from the center, $\Delta\theta$ is the change in angular position, and $\Delta t$ is the time delay between deformed and undeformed line acquisition. The measured velocity may deviate from this value due to motion parallel to the line. For example, flow outward from the center may cause a larger or smaller observed difference in angular location, dependent on the local gradient of tangential velocity with radial location. Hill and Klewicki showed that the error in measuring the component of velocity normal to an MTV line, $u$, is $\Delta u = u\Delta t(v/u)(\partial u/\partial y)$, where $v$ is the velocity parallel to the line and $y$ is the coordinate along the line direction. Thus the errors in determining the tangential and axial velocities are $\Delta V_\theta/V_\theta = \Delta t(V_r/V_\theta)(\partial V_\theta/\partial r)$ and $\Delta V_z/V_z = \Delta t(V_r/V_z)(\partial V_z/\partial r)$, respectively. Clearly the error in the measurement approaches zero as the time delay approaches zero, although some $\Delta t$ is required for the line comparison. The error also decreases as the radial velocity approaches zero and as the gradient of the velocity with respect to $r$ approaches zero. The error will be a maximum when the radial velocity and the gradient velocity component of interest are maximums. The data show that this occurs in the regions of large-velocity gradients next to the prism faces of the rotating crystal. In these regions the radial component will be of similar magnitude as the other two components, and with the exception of the first 1/8 revolution, the largest observed gradients of $V_\theta$ and $V_z$ with respect to $r$ are about 15/s. As rotation continues to steady state the largest observed gradients are about 3–4/s. The maximum error due to flow parallel to the MTV line is thus 7.5% during early time and about 2% at steady state.

Figure 2 is useful in discussing one of the difficulties associated with making velocity measurements for rotating body flows. Because the crystal is rotating relative to a stationary MTV line, the length of the line varies due to the crystal geometry. At $\theta = 0°$ the MTV line extends to the crystal corner, a distance of $L$ from the center of the crystal. As the crystal rotates to $\theta = 45°$, however, the MTV line terminates at the middle of a prism face, a distance of $L/2^{1/2}$ to the center of the crystal. Recall that $L$ is the distance from the center of the crystal to a prism corner in a horizontal plane. The currently used image-analysis algorithm recognizes when the line has terminated at a surface. Thus for each image recorded, and as rotation occurs, the length of the MTV line varies and extends from the moving crystal surface to the extent of the camera view as shown in Figure 2.

The resulting data set is a collection of instantaneous velocity profiles of different lengths (corresponding to crystal position) separated by 1/60 s. From these velocity profiles, time series of the velocity component of interest can be generated at 60 Hz for any fixed point beyond the extent of the crystal corner. In the region between $\theta = 0°$ and $\theta = 90°$, velocity data are obtained at all points before the MTV line terminates at the surface. One advantage that MTV has over point-measurement methods including Laser Doppler Velocimetry (LDV) is that data are obtained for each image regardless of where the MTV line terminates at the surface. The use of LDV or a similar method in the region between $f/2$ and $L$ results in data at a fixed point only when there is no obstruction of one of the laser beams by the rotating crystal.

Because the MTV line is fixed in laboratory coordinates and the crystal is rotating, the tangential velocities are measured with respect to the laboratory frame and not with respect to the rotating crystal. Subtraction of the quantity $\Omega r$ ($\Omega$ is the angular rotation rate, and $r$ is distance from the center of rotation) from each corresponding tangential velocity profile results in velocity profiles that are relative to the rotating crystal. Measurement of the axial velocity profiles in the laboratory reference frame are unchanged when trans-

forming to a reference frame fixed on the crystal, since there is no crystal motion in the axial direction.

## Results

Selected representative measurements of the tangential and axial velocities at $z^* = 0.125$, $z^* = 0.5$, and $z^* = 0.875$ will be presented. The clockwise direction is taken as positive for the tangential velocity, and upward away from the platform is taken as positive for the axial velocity data.

### *Steady-state velocity profiles*

A representative sample of averaged steady-state tangential and axial velocity profiles are shown in Figures 3 and 4. For these data the Reynolds number ($Re = \omega L^2/\nu$) was 1.51 $\times 10^4$ and the rotation direction was clockwise. Mean profiles were computed by ensemble averaging, over 30 ensembles, the obtained velocity profiles every revolution. This was done for several angular locations from $\theta = 0°$ to $\theta = 90°$, where $\theta = 0°$ corresponds to the point when the MTV line terminates at the crystal corner (see Figure 2) and $\theta = 45°$ corresponds to the point when the MTV line terminates at the middle of the prism.

*Tangential Velocity Behavior.* Figure 3a plots the normalized tangential velocity, with respect to the rotating crystal, $V^*_{\theta c} = (V - \Omega_r)/(\Omega L)$ vs. $r^* = (r - f)/(L - f)$ for $z^* = 0.875$, and at angular locations of $\theta = 0$, 9, 27, 45, 63, and 81°. The normalized radial coordinate is $(r - f)/(L - f)$, so that $r^* = 0$ at the prism face and $r^* = 1$ corresponds to the crystal corner. Recall that $f$ is the prism face length. Shown in Figure 3b and 3c is $V^*_{\theta c}$ vs. $r^*$ for the same six angular locations, but at $z^* = 0.5$ (Figure 3b) and $z^* = 0.125$ (Figure 3c). Positive values of $V^*_{\theta c}$ indicate fluid motion clockwise with respect to the crystal, and negative values indicate counterclockwise motion. The rotation direction for all data presented here was clockwise unless otherwise specified. The data of Figure 3a show that at $z^* = 0.875$ a pronounced recirculation region exists for $\theta > 0$. This is illustrated by the double inflectional profiles in the $V^*_{\theta c}$ data. For example, for the $\theta = 45°$ case, $V^*_{\theta c}$ is zero at the crystal surface ($r^* = 0$) and decreases to $V^*_{\theta c} \approx -0.1$ at $r^* \approx 0.1$. Then $V^*_{\theta c}$ increases to about 0.1 at $r^* \approx 0.65$, and then decreases again over the remainder of the $r^*$ region investigated. This behavior is quite similar for the $\theta = 27°$, 45°, 63°, and 81° data, with the only variation being the $r^*$ position, where $V^*$ changes direction. This variation in this $r^*$ location results because of the rotation of the crystal relative to the MTV line. Note that in the region beyond the crystal corner passage point ($r^* \geq 1.0$) that the magnitude and direction of $V^*_{\theta c}$ for all of these cases is similar. The $\theta = 9°$ degree data are different from the other nonzero cases. The difference is that the velocity profile does not exhibit a double inflection. This indicates that the inner recirculation region does not extend over the entire portion of the prism face, but extends to a $\theta$ location somewhere between $\theta = 9°$ and 27°. At $\theta = 0°$ the tangential velocity is about zero for the entire measurement region ($1.0 \leq r^* \leq 1.6$) and differs significantly from the $\theta = 9°$ and 81° data. This suggests that large gradients in the tangential velocity with respect to angular position ($\partial V_{\theta c}/\partial\theta$) exist at angular locations near the corners. Note that the profile terminates at $r^* = 1$, where $V^*_{\theta c}$ goes to zero at the corner.

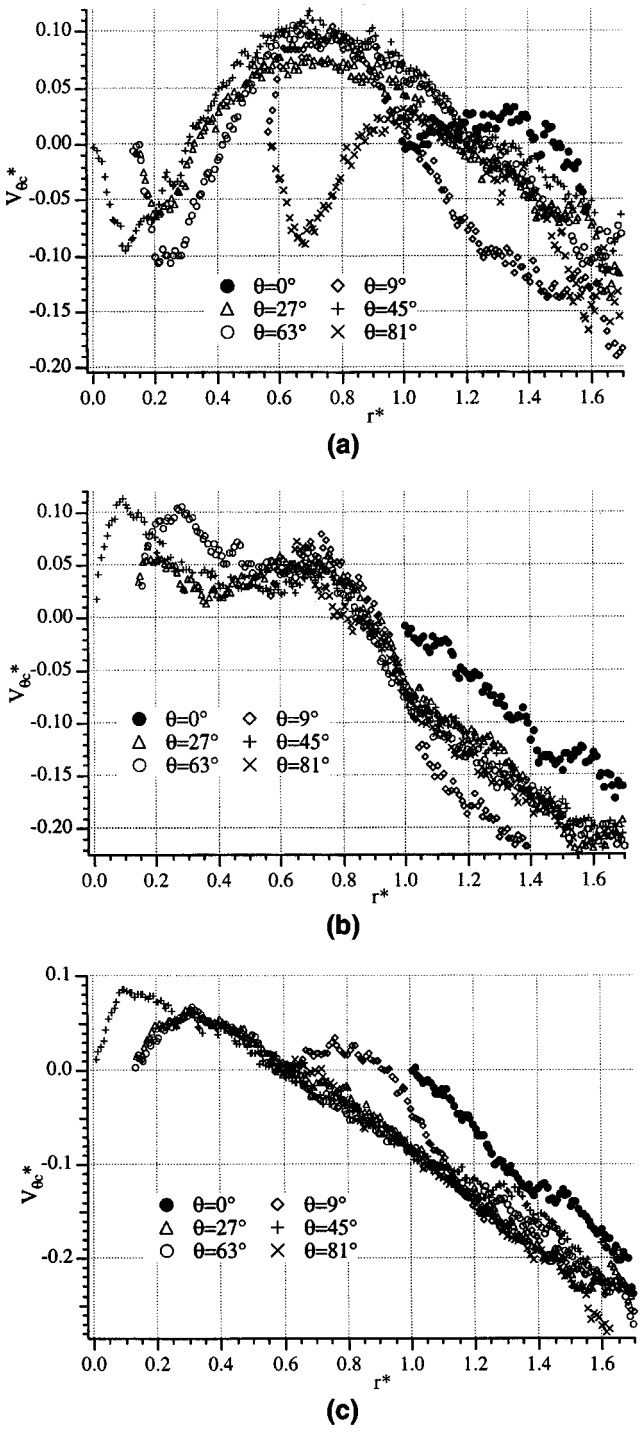


**Figure 3. Average $V^*_{\theta c}$ steady-state profiles at angular locations of 0°, 9°, 27°, 45°, 63°, and 81°, and at the three measurement locations.**

(a) 0.01 m above the platform ($z^* = 0.125$); (b) crystal mid-height ($z^* = 0.5$); and (c) 0.01 m ($z^* = 0.875$) below the top of the prism face.

The $V^*_{\theta c}$ data at $z^* = 0.5$ (Figure 3b) differs from the data at $z^* = 0.875$ in that the velocity profiles do not exhibit the double inflectional behavior described earlier. For all of the nonzero cases, in the $r^* < 1.0$ region, $V^*_{\theta c}$ is positive and rela-

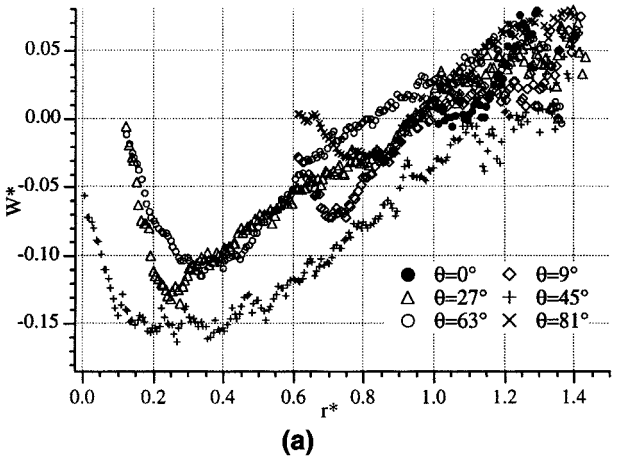


(a)

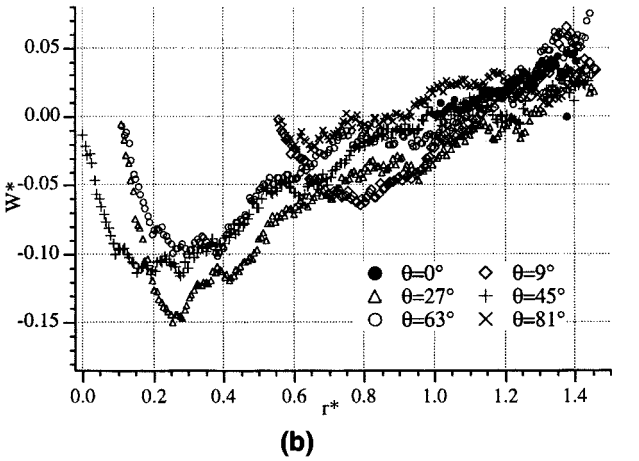


(b)

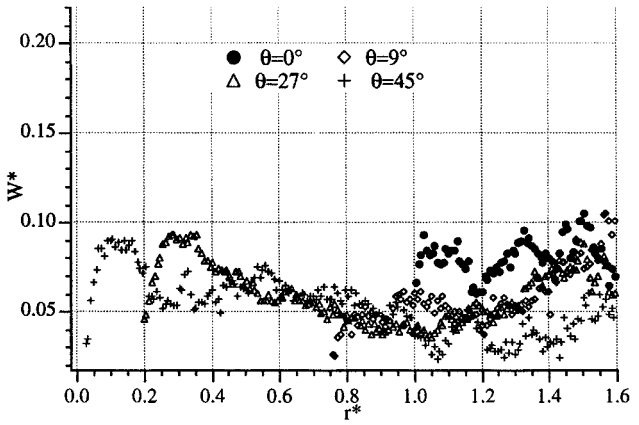


(c)

**Figure 4. Average $W^*$ steady-state profiles at angular locations of 0°, 9°, 27°, 45°, 63°, and 81°, and at the three measurement locations.**

(a) $z^* = 0.125$; (b) $z^* = 0.5$; (c) $z^* = 0.875$.

tively constant until just prior to a decrease to zero in a boundary layer adjacent to the surface. In this region ($0 < r^* \leq 1.0$) the relative tangential velocity is similar in magnitude for all cases and is approximately 5% of $\Omega L$ until $r^* \approx 0.8$. At this point $V_{\theta c}^*$ decreases for all nonzero cases in a similar manner and with similar magnitude. The $\theta = 0°$ data behave similarly, but with smaller magnitude. The data indicate that $\partial V_{\theta c}/\partial\theta$ is small for all $\theta$ except near the passage of the crystal corner. The data also show that with respect to the crystal, the velocity direction for $r^* \geq 1.0$ is negative or counterclockwise.

The $V_{\theta c}^*$ data near the bottom of the crystal (Figure 3c) show slightly different behavior than at $z^* = 0.5$. At this position the $\theta = 27°$, 45°, 63°, and 81° cases are almost identical, with the exception simply being the location on the prism face where the MTV line terminates. For $r^* > 0.6$ and these $\theta$ locations, the value of $V_{\theta c}^*$ decreases from 0 to about $-0.2$ at $r^* \approx 1.6$. At $r^* < 0.6$ $V_{\theta c}^*$ increases linearly until a maximum is reached, where it decreases to zero in the wall boundary layer as shown in the figure. The $\theta = 0°$ data differ from these cases just as they did at the midplane location. The $\theta = 9°$ case also differs at this location, primarily for $0.6 \leq r^* \leq 1.5$, where the value of $V_{\theta c}^*$ is between that for the $\theta = 0°$ data and the other four cases. Recall that $\theta = 9°$ corresponds to the position just after the corner has passed the MTV line.

*Axial Velocity Behavior.* The axial flow data at both $z^* = 0.5$ and $z^* = 0.875$ behave quite similarly. This is shown in Figure 4a and 4b. The primary difference between profiles is the location where the profile ends at the crystal, and the magnitude attained. At almost all $\theta$, $W^*$ is negative, toward the platform, for $r^* < 1.0$ and positive, away from the platform, for $r^* > 1.0$. At $z^* = 0.875$ the largest downward velocity occurs at 45° and is about 15% of the $\Omega L$. At $z^* = 0.5$, the largest downward velocity occurs at 27°, or closer to the crystal corner. The data clearly indicate that all motion toward the platform occurs close to the prism faces ($r^* \leq 1.0$).

Interestingly, the behavior of $W^*$ at $z^* = 0.125$ is upward at all $r^*$, although the magnitude is significantly smaller. Also the $W^*$ data at this location exhibit more fluctuation for a given profile. Measurements of both the tangential and the axial velocity rms were significantly higher at this $z^*$ than at the other $z^*$ locations. Because $W^*$ is upward at this location, it is evidence that a vertical recirculation region exists. This recirculation region exists because the downward flow is decelerated by the platform base below the crystal. Consequently, it would be expected that the axial velocity profiles would be less well behaved in this region.

Note from Figure 1 that the platform has vertical support bars radially outward from two of the crystal corners in addition to a horizontal support bar connecting the vertical bars. The data of Figures 3 and 4 correspond to the prism face prior to the support bar. Measurements next to the face after the support bar show that the magnitude of the maximum velocity in the $r^* \leq 1.0$ region is about 25% greater both for the $V_{\theta c}^*$ data and the $W^*$ data. Aside from this difference the behavior of the data is similar for all $\theta$ and all three vertical measurement locations.

### *Evolution dynamics after after startup or reversal*

Evolution of the flow field from startup will now be discussed. Presented in Figure 5 are measurements of the normalized instantaneous tangential ($V_{\theta c}^* = (V(t) - \Omega r)/\Omega_f L$) (Figure 5a) and axial ($W^* = W(t)/\Omega_f L$) (Figure 5b) velocities as a function of time, at two radial locations and at the $z^* = 0.125$ position. The final rotation rate is represented by $\Omega_f$.

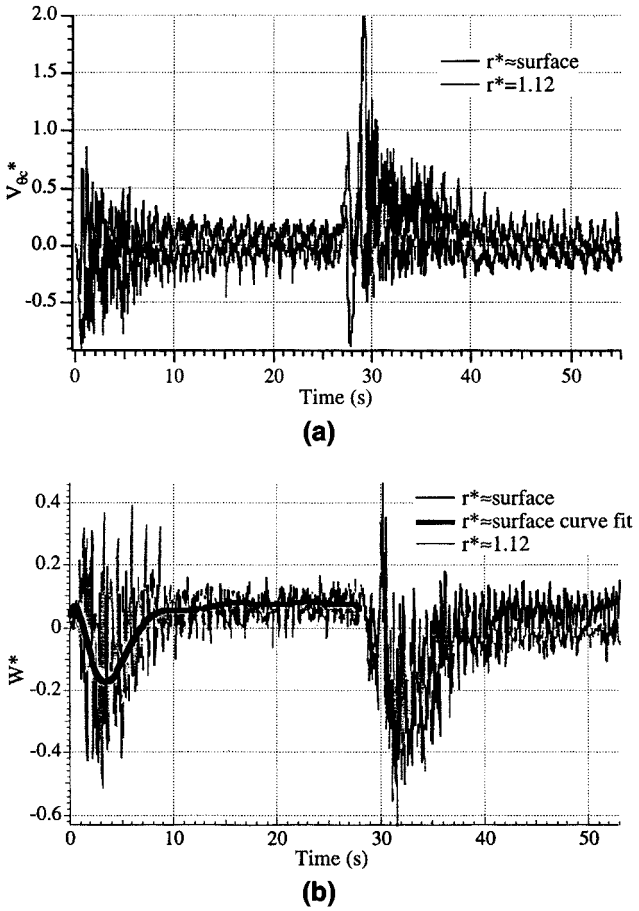


**Figure 5. Temporal evolution of (a) the crystal reference frame tangential velocity, $V_{\theta c}^*$, and (b) velocity, $W^*$, near the crystal surface and at $r^* = 1.12$ beyond the crystal corner.**

The data correspond to $z^* = 0.125$, $\omega = 0.75$ rps, and $\alpha = 1.0$ rps$^2$, and covers two periods including the discontinuation of rotation at 27.5 s and reversal of direction at 28.5 s.

The data represent two time series with subsequent values separated by 1/60 of a second. Although at first it may appear that there is a lot of noise in the transient measurements, the fluctuations in the velocity field represent real behavior and the measurements are very repeatable. The large variations correspond to the fluid motion caused by the passage of crystal corners past the MTV line location. The first measurement location was at a fixed laboratory angular position and at a fixed distance relative to the crystal surface of about 10 pixels ($\sim 0.7$ mm). The second location is at the same angular position, but at a fixed radial position of 30 pixels ($\sim 2$ mm) beyond the extent of the crystal corner, $r = L + 2$ mm ($r^* \approx 1.12$). Because at the first location the distance relative to the crystal is fixed, the actual measurement location varies radially as the crystal rotates, so that the velocity data do not correspond to a fixed point in space, but correspond to a fixed distance from the rotating mock crystal.

The Reynolds number and nondimensional acceleration rate ($\alpha^* = \alpha/\Omega^2$) were $1.5 \times 10^4$ and 1.8, respectively. The figure (Figure 5a) shows that near the crystal surface the flow direction is generally positive with respect to the crystal and at $r^* \approx 1.12$ the direction is generally negative. After the first 5 s or 3.5 revolutions, $t^*$, $V_{\theta c}^*$ changes very little in magnitude, in an average sense, next to the crystal surface. After 10 s ($t^* \approx 7$), $V_{\theta c}^*$ at $r^* \approx 1.12$ also exhibits little change in an average sense. At all locations, the magnitude of $V_{\theta c}^*$ is the largest during the first 10 s and large fluctuations are prevalent. It is a maximum after about 0.5 s, and decreases as the fluid is spun up to the speed of the crystal. Some regular periodicity in the data is observed above $t = 10$ s.

At $t = 27.5$ s ($t^* = 20$) rotation is stopped, the crystal remains stationary for 1 s, and then reverses direction. When the crystal stops $V_{\theta c}^*$ attains its largest magnitude (2.0 near the crystal surface) and exhibits large variation in magnitude and direction during the rest period. Upon reversal of direction, the behavior is similar to the behavior after startup, except the magnitude of $V_{\theta c}^*$ at $r^* \approx 1.12$ is larger for the first 10 s than during the initial period. After reversal of motion the behavior is markedly similar to the evolution after startup in an initially quiescent fluid. Indeed subsequent reversals exhibit similar behavior as that shown for the first reversal.

The behavior and evolution of $W^*$ is markedly different from $V_{\theta c}^*$ and is described. Immediately after startup $W^*$ exhibits fluctuations in magnitude between $-0.3$ and 0.4, both near the crystal surface and at $r^* \approx 1.12$, and the behavior is similar at both locations. During this initial period, the data show fluctuation between positive and negative values. When considering the instantaneous velocity behavior, for $t < 7$ s, the direction is downward after the passage of each corner (the leeside of the corner), but positive just prior to the next corner. Negative axial flow is induced by the low-pressure region on the leeside of the corner and positive flow is caused by the next corner acting to push fluid out of its way. In an average sense (average over the crystal surface) the flow direction is negative (downward), as shown by a least-squares fit of the near surface data covering the initial period. Note that in a average sense the maximum downward velocity is attained at about $t = 3.5$ s ($t^* \approx 1.6$), where $W^* \approx -0.2$. Above $t \approx 7$ s ($t^* \approx 5$) the curvie fit of the $W^*$ data remain positive at a value close to 0.08 until rotation ceases, at which point large fluctuations again occur. Upon reversal of direction by the crystal, the evolution of the $W^*$ data is similar to the evolution for the initial period, with two distinct differences. The first difference is that in an average sense $W^*$ reaches a maximum magnitude of about $-0.3$, or 50% higher than for the initial period. The second difference is that after the fluctuations have decreased the average of $W^*$ near the crystal surface is upward as for the initial period, but is approximately zero at the location beyond the crystal corner. This is indicative of a vertical separated flow zone that exists near the junction of the prism faces with the horizontal platform. Subsequent reversals exhibit very similar behavior to the post reversal data of Figure 5b. It is interesting to point out that in an average sense, regardless of the direction of rotation or the rotation rate, $W^*$ decrease to a maximum downward value close to $-0.3$ at $t^* \approx 1.5$ and this $z^*$. For larger $t^*$, $W^*$ increases to a relatively constant value. For the data of Figure 5b this value is upward near the crystal, whereas at $z^* = 0.5$ and $z^* = 0.875$ the direction is downward.

Although the tangential velocity changes direction with each reversal, and thus relative motion between the crystal

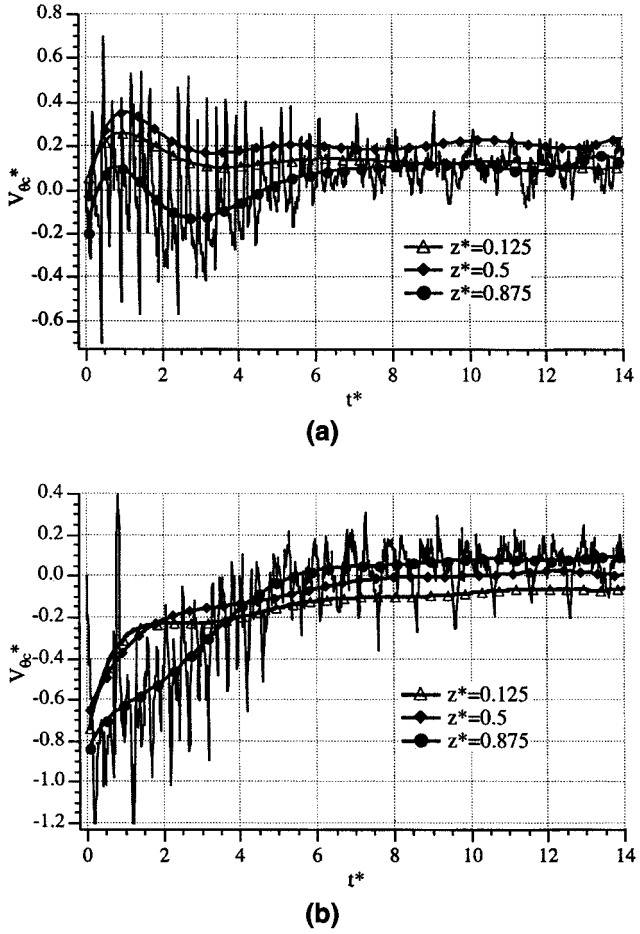


**Figure 6. Evolution of $V_{\theta c}^*$ vs. $t^*$ (a) near the surface of the rotating crystal and (b) at $r^* = 1.12$ cm for vertical locations of $z^* = 0.125$ $z^* = 0.5$, and $z^* = 0.875$.**

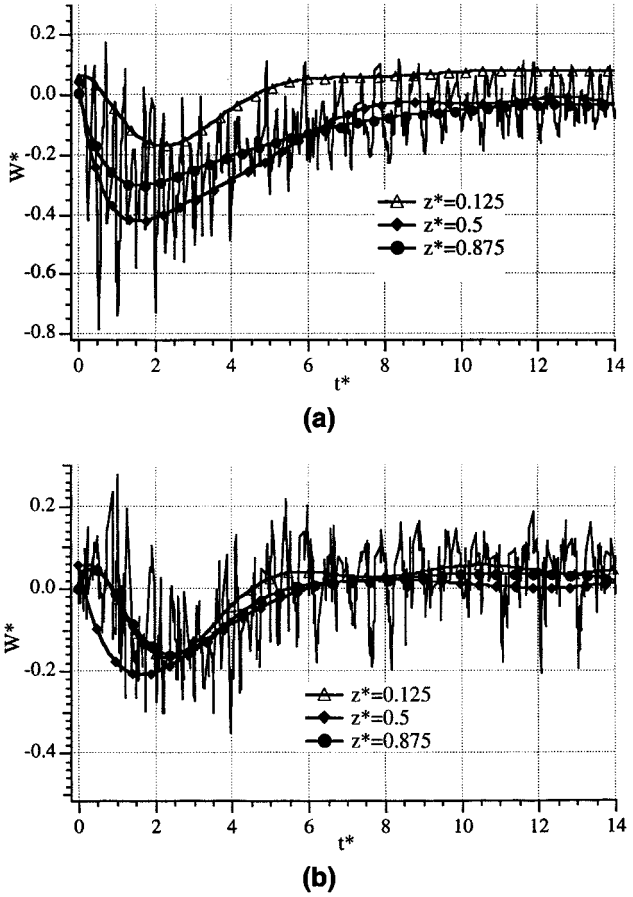


**Figure 7. Evolution of $W^*$ vs. $t^*$ (a) near the surface of the rotating crystal and (b) at a fixed radial location of $r^* = 1.12$ for vertical locations of $z^* = 0.125$, $z^* = 0.5$, $z^* = 0.875$.**

and the fluid reverses with each reversal, the axial velocity does not reverse direction with each reversal, but on average is downward after each reversal of direction. The fluctuations in both $V_{\theta c}^*$ and $W^*$ result due to the nature of turbulent flow and the periodicity of the passing crystal corners. Measurements with $Re$ varying from $4\times10^3$ to $3\times10^4$ with $\alpha^* = 1.8$ exhibited similar temporal behavior as shown in Figures 5a and 5b. The values of $V_{\theta c}^*$ and $W^*$ over this range of $Re$ were almost identical to the data of Figures 5a and 5b for the entire rotation period.

### *Spatial variation in $V_{\theta c}^*$ and $W^*$*

Variations in the evolving $V_{\theta c}^*$ and $W^*$ data with vertical and radial position are now addressed. Figure 6 presents a time series of the $V_{\theta c}^*$ data corresponding to the $z^* = 0.875$ measurement location, at a radial position fixed at 2 mm from the crystal surface (Figure 6a), and at the fixed radial location of $r^* = 1.12$ (Figure 6b). Also shown is a ninth-order polynomial least-squares curve fit to illustrate the evolution of the mean flow field. Similar curve fits are shown on the figure for the $V_{\theta c}^*$ data at $z^* = 0.5$ and 0.125. The instantaneous velocities are not shown for clarity. Likewise Figure 7 shows the $W^*$ data at the same locations and presented in the same manner. Both $V_{\theta c}^*$ and $W^*$ are plotted vs. the number of revolutions, $t^*$, and represent startup from rest until a mean flow steady state is obtained at each location. For subsequent reversals of direction the data behave in a manner similar to that shown in Figures 6 and 7, with differences only in magnitude of $W^*$ as discussed in the previous subsection. The data of Figure 6 show that the evolution of $V_{\theta c}^*$ at $z^* = 0.125$ and $z^* = 0.5$ are very similar over the entire period, both near the surface and at $r^* = 1.035$. The mean value of these nondimensional velocities is slightly greater for the $z^* = 0.5$ data over the entire period.

The behavior of $V_{\theta c}^*$ at $z^* = 0.875$ differs from the behavior at $z^* = 0.125$ and $z^* = 0.5$ mainly for $t^* < 6.0$. Above $t^* \approx 6.0$ the behavior of the tangential velocity appears to be quite similar to the other locations. Below $t^* \approx 6.0$ the magnitude of $V_{\theta c}^*$ at $z^* = 0.875$ is smaller and it takes slightly more revolutions to reach the steady-state value of the average velocity. This is due to the taper of the pyramidal cap corresponding to smaller induced velocities above the prism. The magnitude of the fluctuations in the instantaneous $V_{\theta c}^*$ data is about the same at all position, both near the surface and at $r^* = 1.035$.

The data of Figure 7 show that for $r^* = 1.12$ the evolution and behavior of $W^*$ is similar for all three $z^*$ (Figure 7b). On average the most downward value of $W^*$ $(-0.2)$ is attained at $t^* \approx 2.5$ and levels off close to zero after $t^* \approx 6$ revolutions. Near the crystal surface, however, the mean values at the three locations are slightly different (Figure 7a). For $t^* < 5$ the direction of the mean axial flow is downward for all three $z^*$. For $z^* = 0.125$ $W^*$ is the smallest in magnitude and largest for $z^* = 0.5$ in this $t^*$ range. Just after initiation of motion ($t^* \approx 1-5$), the curve fit of the $W^*$ data at $z^* = 0.5$ exhibits a maximum magnitude of about $-0.4$. For $z^* = 0.875$, the maximum magnitude of $W^*$ is about $-0.3$ and occurs at $t^* \approx 2.0$.

The data thus suggest that during the initial period ($t^* < 6.0$) the axial flow accelerates over the top portion of the prism but decelerates as the platform is approached. Above $t^* \approx 6$ the magnitude of $W^*$ is similar at both $z^* = 0.5$ and $z^* = 0.875$. The direction of the mean velocities is downward over the entire rotation schedule at these two locations, but approaches a small value at steady state (see the subsection on steady-state velocity profiles). For $z^* = 0.125$, as steady state is approached, the mean axial flow near the crystal surface is upward due to the existence of a vertical recirculation region. Like the $V_{\theta c}^*$ data, the fluctuations of $W^*$ about the mean are similar at all vertical locations. Recall that upon reversal the maximum values of $W^*$ are about 50% higher than those shown in Figure 7.

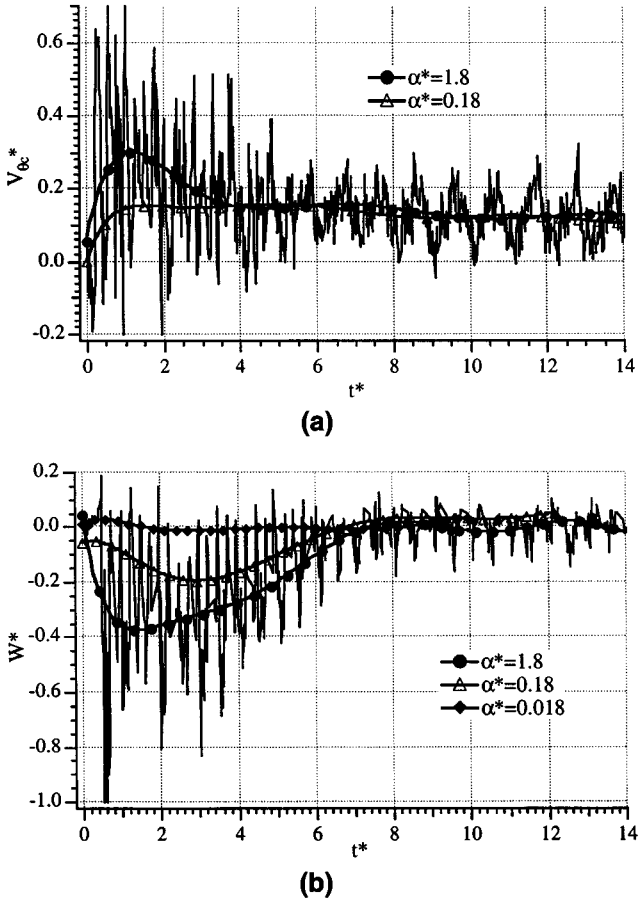


**Figure 8. Evolution of (a) the relative tangential velocity and (b) axial velocity vs. $t^*$ near the surface of the rotating crystal, at $z^* = 0.125$, and at three angular accelerations.**

### *Effects of angular acceleration*

The effects of the angular acceleration on the behavior of the velocity field show some very interesting trends. Figure 8 presents the evolution of $V_{\theta c}^*$ (Figure 8a) and $W^*$ (Figure 8b) from startup to $t^* = 14$ near the crystal surface and at $z^* = 0.5$ for three $\alpha^*$ (0.018, 0.18, 1.8). The final Reynolds number was $1.51 \times 10^4$ for all cases and the dimensional accelerations were 0.01, 0.1, and 1.0 rps$^2$. The data of Figure 8a are somewhat surprising as they indicate that after motion has initiated there is little change in the average value of $V_{\theta c}^*$ for the entire period. The $V_{\theta c}^*$ data for all three $\alpha$, differing by two orders of magnitude, are almost identical. Data for $\alpha^* = 0.018$ are not shown on the figure because they are virtually identical to the $\alpha^* = 0.18$ data. Small differences exist in the data right after startup, but in general the data are similarfor all $\alpha^*$ and the magnitude of the mean values of $V_{\theta c}^*$ remain approximately constant over the entire rotation period. For all $\alpha$ and $\omega$ investigated the velocity data exhibit the same periodicity with $t^*$ as shown in Figure 8a.

The $W^*$ data show markedly different behavior and are shown in Figure 8b. For all three $\alpha^*$, after about $t^* \approx 8$, the magnitude and behavior of $W^*$ is similar. For $t^* < 8$, however, large differences exist when comparing the three data sets. At early $t^*$, $W^*$ is greatest for $\alpha^* = 1.8$ and is the smallest for $\alpha^* = 0.018$. In fact, for $\alpha^* = 0.018$, $W^*$ remains close to zero over the entire rotation schedule. For $\alpha^* = 0.18$ and 1.8, the magnitude of $W^*$ increases with increasing $\alpha^*$, although not in a proportional manner. For these two cases $W^*$ is a maximum at early $t^*$ and then decreases to values fluctuating around zero.

## Discussion

### *Flow-field description from startup*

The behavior of $V_{\theta c}^*$ and $W^*$ from startup, or after rotation reversal, including acceleration effects and spatial variations, can be summarized by the following observations.

- The average values of $V_{\theta c}^*$ do not depend upon $\alpha^*$, but at a fixed location with respect to the rotating crystal, remain relatively constant for all $\alpha^*$ and *Re* explored.
- The relative axial velocity does depend strongly on $\alpha^*$ at early $t^*$, increasing with increasing $\alpha^*$.
- In an average sense the axial velocity increases to a maximum directed toward the platform just after reversal, or startup, but then decreases toward smaller magnitude as steady state is approached.
- Instantaneously, $W^*$ depends on $\theta$ and is negative just after a corner passage, but positive just prior the next corner passage for $t^* \leq 7$.
- At steady state, $W^*$ $(r^* < L^*)$ is negative at $z^* = 0.5$ and $z^* = 0.875$ for all $\theta$ with the magnitude decreasing as the crystal corner approaches.
- A vertical recirculation of the axial flow occurs near the junction of the prism faces and platform surface.
- Upon reversal of rotation, the average $V_{\theta c}^*$ also reverses direction, but in an average sense $W^*$ is always downward

with the exception of a small region near the platform, where it is upward.

- For all reversals of rotation the curve fit of the $V_{\theta c}^*$ data attains a similar magnitude, but $W^*$ attains a magnitude 50% higher than for the initial period.

The evolution of the flow field from startup is now described. As the crystal begins to rotate in an initially quiescent fluid, or after reversal of rotation direction, large axial velocities are induced by the crystal owing to low-pressure regions that exist in the core of the separated flow near the crystal faces. Near the platform the axial flow is converted to radial outflow. This pumping of the solution is driven largely by the crystal and should not be confused with transport caused by the formation of an Ekman layer in a spinning tank, discussed in detail by Wedemeyer (1964). Solution that is transported in the axial direction largely consists of a fluid with a component of $\theta$-momentum that is close to zero or opposite in sign of the rotation direction. Consequently, the tangential velocity gradients near the crystal do not decrease but remain large; and the regions of separated flow extend out to the crystal corners as observed from flow visualization. As a result the velocity fluctuations in the region near the crystal faces remain approximately constant. For low $\alpha$, the relative velocity is much smaller initially, and thus size of the separated regions is much smaller, as are the velocity gradients.

After some characteristic time, based on rotation rate, and geometric parameters, turbulent motions have convected over the entire tank volume and the relative velocity near the rotating crystal begins to decrease. A time scale describing this behavior has been developed previously for a rotating bluff body (Maynes et al., 1999). The fluid now being transported toward the body in the established secondary flow now has some angular momentum in the direction of rotation, and as a result the velocity gradients near the crystal decrease. As rotation continues the velocity gradients and fluctuations continue to decrease until steady state is attained.

Theory by Greenspan and Howard (1963) show that for spin-up of a fluid in a cylindrical tank, the spin-up time is $t = H^2/(\nu\Omega)^{1/2}$, where $H$ is the tank height, and $\Omega$ is the rotation rate. For the tank employed for this study and the same rotation rate of 0.75 rps, the spin-up time would be 117 s. The temporal evolution from startup to steady state for a rotating crystal on a platform is significantly different from spin-up of a fluid in a circular cylinder. For the latter, the flow field is driven by turbulent motions generated at the crystal corners and platform support bars. For the present data, steady state, when considering startup in a quiescent fluid, is attained at $t^* = 12$ or $t = 16.4$ s. When considering rotating bluff bodies without a platform, the spin-up time has been shown to be a function of tank height, tank radius, body height, and body aspect ratio (Maynes et al., 1999).

Figure 9 depicts the qualitative behavior of the velocity field for an $r$-$z$ plane and in the region of the crystal surfaces. The solid lines depict the expected $r - z$ plane velocities based upon the velocity data. The dashed lines represent fluctuations in the velocity due to the crystal geometry. These fluctuations are superimposed on the average velocity for a qualitative description of the behavior at a given point. All of the obtained data suggest that with few exceptions the average velocity is downward at all points except near the junction of the platform and the prism faces, where a separated region is believed to exist and is depicted on the lower panel. The largest downward velocities were measured following the passage of a corner (at prism midplane) and the minimum downward velocity occurs immediately prior to the corner passage. That Figure 9 is an accurate portrayal of the flow field is evidenced by all of the obtained data.

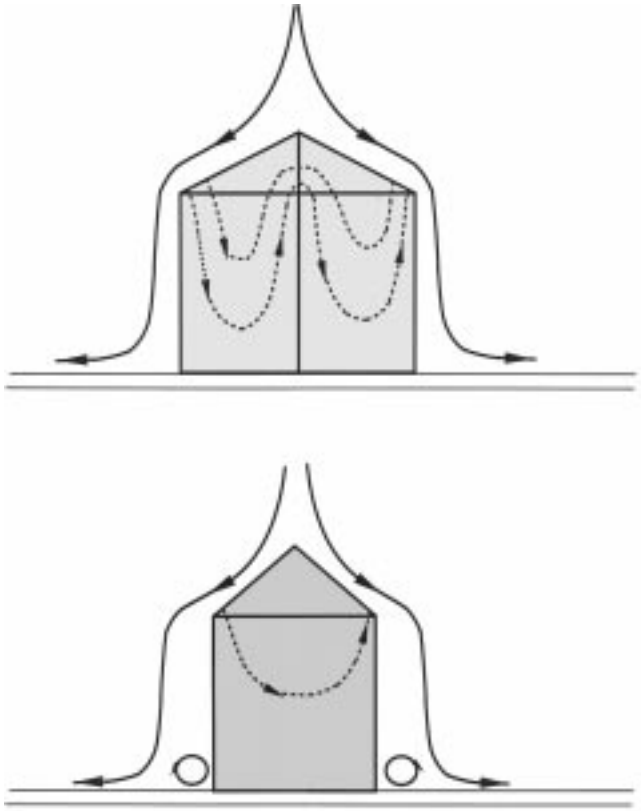

**Figure 9. Flow-field of the axial velocity flow patterns near the crystal for a crystal on a platform rotating in a tank.**

The bottom panel corresponds to a view normal to a prism face, and the top panel is a view normal to a prism corner.

### *Significance to rapid crystal growth*

The presented velocity data are significant for validation of full field CFD simulations of crystal-growth environments and also give insights into the formation of inclusions on growing crystals. In general, it can be inferred that as the shear rate on a crystal surface decreases, the rate of mass transfer will also decrease. The shear rate is proportional to $1/\delta$, where $\delta$ is the momentum boundary layer and the mass transfer is proportional to $\delta_c$, where $\delta_c$ is the concentration boundary layer. Both $\delta$ and $\delta_c$ decrease as the characteristic velocity increases, and it has been observed that as the rotation rates increase, crystal growth rates increase (Wilcox, 1983). Observations of growing crystal surfaces show that the growth rate normal to a given surface remains constant across the surface. Consequently, if there exist regions on the crystal surfaces where the shear rate is low relative to the rest of the surface, the concentration of solute at the surface for these

locations can be lower than at regions of high velocity gradients. Prolonged exposure to low shear rate can thus ultimately lead to instability in the growth process, resulting in inclusion formation on the crystal surfaces. Also of importance regarding rapid crystal growth hydrodynamics is the magnitude and behavior of the turbulent fluctuations in the fluid. It is the turbulent motions that largely control the convective mixing that occurs in the solution.

Prediction of inclusion location is impossible without knowledge of the crystal-growth kinetics. For example, the location of the growth hillock and the direction of step propagation are critical. However, the solution velocity magnitude and direction are also critical. Thus, examination of the data can help predict where and explain why inclusions will form given known rotational parameters and growth kinetics.

The velocity data suggest that at low $\alpha$ the relative axial and tangential velocities are always very small. This leads to small velocity gradients at the crystal faces and small turbulent fluctuations in the velocity field. Thus as $\alpha$ is decreased, the boundary-layer thickness on the crystal surfaces decreases and the amount of convective mixing by turbulent motions also decreases. Both effects increase the likelihood of inclusion formation. The data also suggest that if rotation persists for a long time after steady state is attained ($t^* = 12$ for the current data), the relative velocities, and thus surface shear rates, will be smallest in magnitude between $\theta = 63°$ and 90°. Rotation for a long time also results in a much smaller intensity of the turbulent fluctuations (Maynes et al., 1997). Consequently, for unidirectional rotation, inclusion formation could be enhanced in the region between $\theta = 63°$ and 90° because of low relative velocity (just prior to the crystal corner), or inclusion formation may be enhanced due to poor global mixing. Furthermore, the present data show that a vertical recirculation zone exists near the bottom of the crystal, just above the platform. This recirculation zone exists for the entire rotation schedule, and thus in this region the solution can become starved of solute material. Because of this recirculation zone, there always exists an area where the axial velocity will always be small (near the stagnation point of the recirculation zone).

Observations of multiple crystal growths confirm that at high growth rates ($\sim 15$ mm/day) and low accelerations ($\alpha = 0.01$ rps$^2$) inclusions predictably form on the prism faces and near the tops of the pyramidal cap faces. Although velocity data are not available in the pyramidal cap region, it is evident from geometry considerations that the relative dimensional tangential velocity will be much smaller near the top of the pyramid simply because the characteristic radial length and thus driving velocity will be smaller. Further velocity data are needed in the region of the pyramidal cap. Additionally observation shows that inclusions predictably form on the prism faces if rotation occurs in one direction too long. Observations also show that if the rotation rate is too low ($\leq 0.25$ rps), inclusions will generally always form and that a common location of inclusion formation is near the bottom of the prism face.

## Conclusion

At high supersaturation the growth process of KDP crystals is much more dependent upon the velocity field than at lower growth rates. The presented measurements of the tangential and axial velocity show the behavior of these components of velocity at steady state and during the transient process at three vertical locations. The present data represent the first measurements of fluid velocities around rotating crystal geometries. The data provide a benchmark for future computer simulations of the crystal-growth process at higher *Re* than previously obtainable. Rotational conditions and locations on the prism faces where low shear rates are likely to occur have been discussed qualitatively, based on the present measurements. The data suggest that for increased control of the hydrodynamics associated with rapid crystal growth, low acceleration rates should be avoided, since these result in small relative axial and tangential velocities for the entire rotation schedule. Also, rotation in one direction longer than $t^* \approx 12$ for the current geometry will result not only in poor mixing dynamics but also a minimization of the relative velocities. Because $V_{\theta c}^*$ and $W^*$ are proportional to the rotation rate, the data also suggest that increased rotation rates lead to larger axial and relative tangential velocities.

## Acknowledgment

This work was funded by Lawrence Livermore National Laboratory under Contract #B335830.

## Literature Cited

Bertrand, J., J. P. Couderc, and H. Angelino, ''Power Consumption, Pumping Capacity and Turbulence Intensity in Baffled Stirred Tanks: Comparison Between Several Turbines,'' *Chem. Eng. Sci.*, **35**, 2157 (1980).

Bordui, P. F., and S. Motakef, ''Hydrodynamic Control of Solution Inclusion During Crystal Growth of $KiTOPO_4$ (KTP) from High Temperature Solution,'' *J. Cryst. Growth*, **96**, 405 (1989).

Chernov, A. A., ''Stability of Faceted Shapes,'' *J. Cryst. Growth*, **24/25**, 11 (1974).

Coriell, S. R., B. T. Murray, A. A. Chernov, and G. B. McFadden, ''Step Bunching: Generalized Kinetics,'' *J. Cryst. Growth*, **183**, 669 (1998).

De Yoreo, J. J., Z. U. Rek, N. P. Zautseva, B. W. Woods, ''Sources of Optical Distorion in Rapidly Grown Crystals of $KH^2PO_4$,'' *J. Cryst. Growth*, **166**, 291 (1996).

Gendrich, C. P., and M. M. Koochesfahani, ''A Spatial Correlation Technique for Estimating Velocity Fields Using Molecular Tagging Velocimetry (MTV),'' *Exp. Fluids*, **22**, 67 (1996).

Greenspan, H. P., and L. N. Howard, ''On a Time-Dependent Motion of a Rotation Fluid,'' *J. Fluid Mech.*, **17**, part 3, 385 (1963).

Hill, R. B., and J. C. Klewicki, ''Data Reduction Methods for Flow Tagging Velocity Measurements,'' *Exp. Fluids*, **20**, 142 (1996).

Janssen-van Rosamalen, R., and P. Bennema, ''The Role of Hydrodynamics and Supersaturation in the Formation of Liquid Inclusions in KDP,'' *J. Cryst. Growth*, **42**, 224 (1977).

Maynes, D., J. Klewicki, P. McMurtry, and H. Robey, ''Hydrodynamic Scalings in the Rapid Growth of Crystals from Solution,'' *J. Cryst. Growth*, **178**, 545 (1997).

Maynes, D., J. Klewicki, and P. McMurtry, ''Time Resolved Torque of Three-Dimensional Bluff Bodies in a Cylindrical Tank,'' *J. Fluids Eng.*, **120**, 23 (1998).

Maynes, D., J. Klewicki, and P. McMurtry, ''Spin-Up in a Tank Induced by a Rotating Bluff Body,'' *J. Fluid Mech.*, **388**, (1999).

Miller, S., ''Photochemical Reaction for the Study of Velocity Patterns and Profiles,'' BASc Thesis, Univ. of Toronto, Toronto, Ont. Canada (1962).

Nye, J. F., *Physical Properties of Crystals*, Chap. 13, Oxford Univ. Press, New York (1985).

Ponce, A., P. A. Won, J. J. Way, and D. G. Nocera, ''Intense Phosphorescence Triggered by Alcohols Upon Formation of a Cyclodextrin Ternary Complex,'' *J. Phys. Chem.*, **97**, 11137 (1993).

Potapenko, S. Y., ''Morphological Instability of Steps During Crystal Growth from Solution Flow,'' *J. Cryst. Growth*, **158**, 346 (1996).
Rashkovich, L. N., and B. Y. Shekunov, ''Morphology of Growing Vicinal Surface; Prismatic Faces of ADP and KDP Crystals in Solution,'' *J. Cryst. Growth*, **100**, 133 (1990).
Rutherford, K., M. S. Mahmoudi, K. C. Lee, and M. Yianneskis, ''The Influence of Rushton Impeller Blade and Disk Thickness on the Mixing Characteristics of Stirred Vessels,'' *Trans. IChemE.*, **74**, Part A, 369 (1996).
Schulz-Dubois, E. O., ''Accelerated Crucible Rotation: Hydrodynamics and Stirring Effect,'' *J. Cryst. Growth*, **12**, 81 (1971).
Tatterson, G. B., *Fluid Mixing and Gas Dispersion in Agitated Tanks*, McGraw-Hill, New York (1991).
Wedemeyer, E. H., ''The Unsteady Flow Within a Spinning Cylinder,'' *J. Fluid Mech.*, **20**, part 3, 383 (1964).
Wilcox, W. R., ''Influence of Convection on the Growth of Crystals from Solution,'' *J. Cryst. Growth*, **65**, 133 (1983).
Wu, H., and G. K. Patterson, ''Laser-Doppler Measurements of Turbulent-Flow Parameters in a Stirred Tank,'' *Chem. Eng. Sci.*, **44**, (10), 2207 (1989).
Yeckel, A., Y. Ahou, M. Dennis, and J. J. Derby, ''Three-Dimensional Computations of Solution Hydrodynamics During the Growth of Potassium Dihydrogen Phosphate II. Spin Down,'' *J. Cryst. Growth*, **191**, 206 (1998).
Zaitseva, N. P., J. J. De Yoreo, M. R. Dehaven, R. L. Vital, K. E. Montgomery, M. Richardson, and L. J. Atherton, ''Rapid Growth of Large-Scale (40-55 cm) KH2PO4 Crystals,'' *J. Cryst. Growth*, **180**, 255 (1997).
Zhou, Y., and J. J. Derby, ''Three-Dimensional Computations of Solution Hydrodynamics During the Growth of Potassium Dihydrogen Phosphate I. Spin Up and Steady Rotation,'' *J. Cryst. Growth*, **180**, 497 (1997).

*Manuscript received Apr. 5, 1999, and revision received Oct. 12, 1999.*